nature research

https://doi.org/10.1038/s41563-020-00806-2

Supplementary information

Towards chirality control of graphene nanoribbons embedded in hexagonal boron nitride

In the format provided by the authors and unedited

Supplementary Materials for

Towards Chirality Control of Graphene Nanoribbons Embedded in Hexagonal Boron Nitride

Hui Shan Wang[1,2,3,15], Lingxiu Chen[1,3,15], Kenan Elibol[4,5,15], Li He[6,15], Haomin Wang[1,2,3*], Chen Chen[1,2,3], Chengxin Jiang[1,3,7], Chen Li[8,9], Tianru Wu[1,3], Chun Xiao Cong[10], Timothy J. Pennycook[4,9], Giacomo Argentero[4], Daoli Zhang[6], Kenji Watanabe[11], Takashi Taniguchi[11], Wenya Wei[12,13], Qinghong Yuan[12,13], Jannik C. Meyer[4,14*], Xiaoming Xie[1,2,3,7]

Correspondence to: hmwang@mail.sim.ac.cn (H. Wang); jannik.meyer@uni-tuebingen.de (J. C. Meyer)

This PDF file includes:

Supplementary Figures

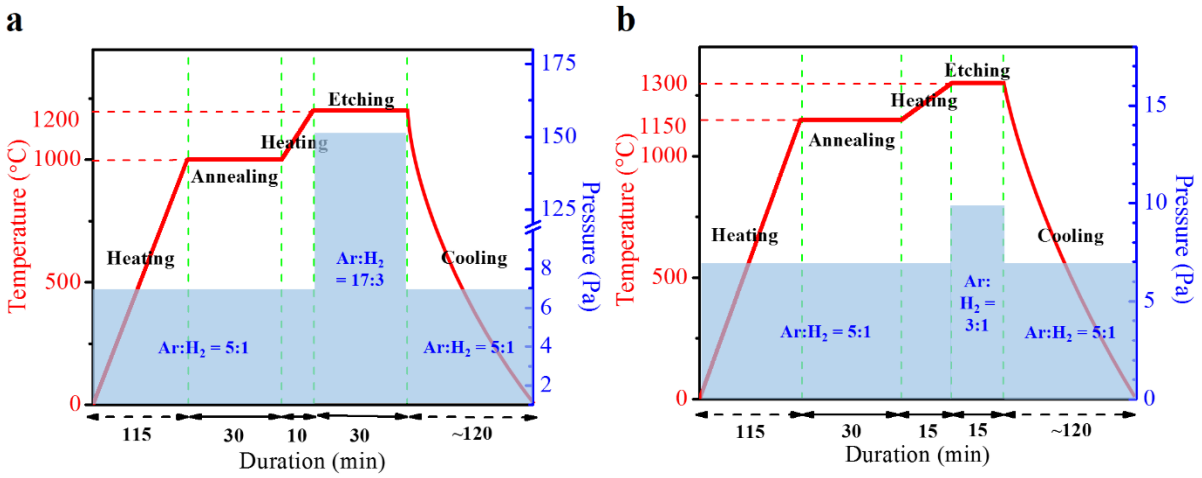

Fig. S1. Schematic diagrams of typical processes for catalytic etching on *h*-BN. (a) A typical etching process for ZZ oriented trenches. The $NiCl_2$-coated samples were submitted to a two-step process: annealing at 1,000 °C for 30 min and etching at 1,200 °C for 30 min under an Ar:H_2 flow (850:150 sccm), and the etching pressure was kept at ~150 Pa. **(b)** A typical etching process for AC oriented trenches. The H_2PtCl_6-coated samples were annealed at 1,150 °C for 30 min and etched at 1,300 °C for 15 min under an Ar:H_2 flow (30:10 sccm) with the etching pressure ~10 Pa. The pressure during heating, annealing and cooling process for both system was kept at ~7 Pa with an Ar:H_2 (10:2 sccm) flow.

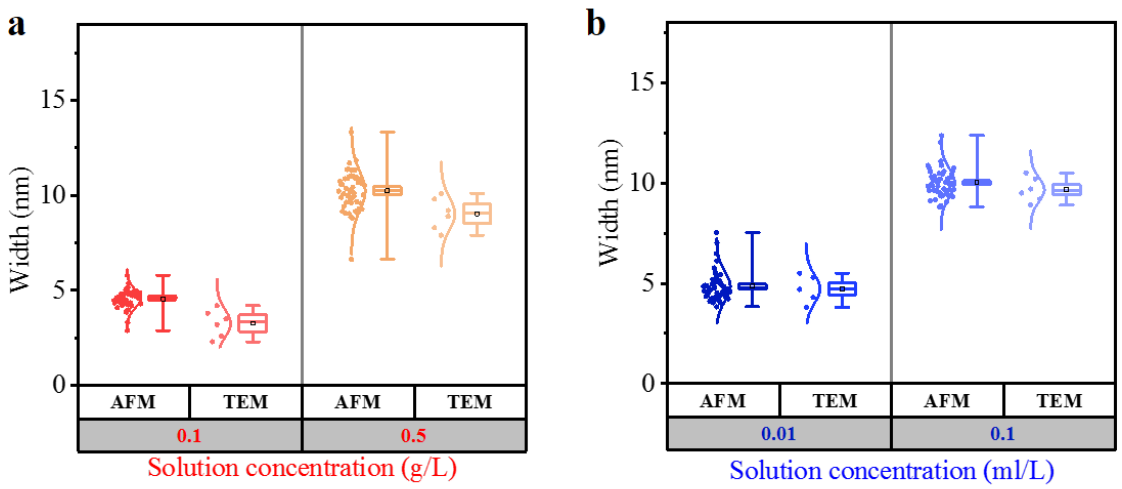

Fig. S2. Boxplots of trench width distributions under optimized etching conditions. (a) Width distribution of the zigzag-trenches obtained at 1200 °C. **(b)** Width distribution of armchair trenches obtained at 1300 °C.

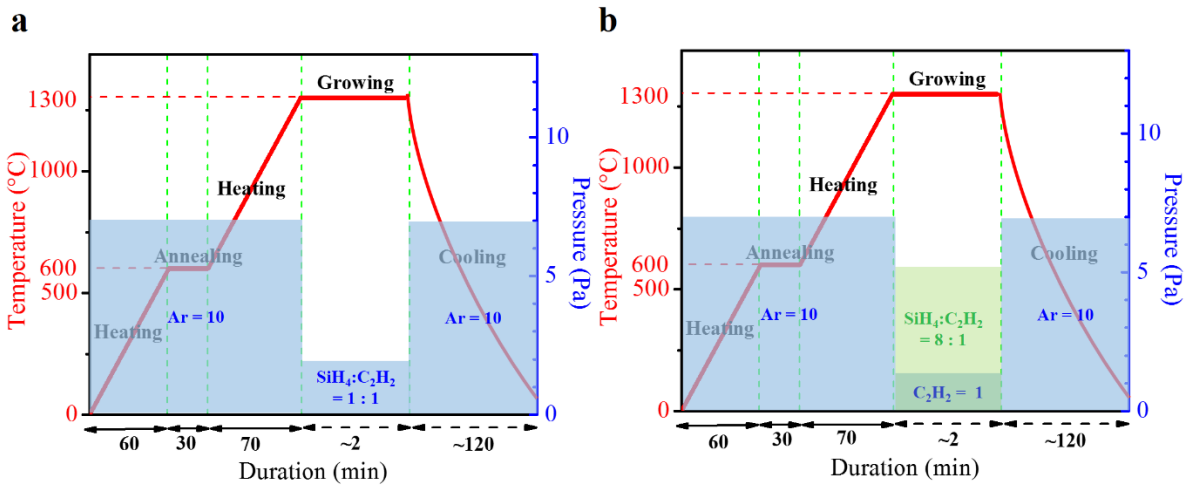

Fig. S3. Schematic diagrams of edge-specific GNR growth on *h*-BN. (a) A typical process for ZGNR growth. Before GNR growth, the samples were first heated to 600 °C to remove contaminants. The ratio of silane to C_2H_2 was ~1:1, the pressure was maintained at ~2 Pa during the growth. **(b)** A typical process for AGNR growth. After heating, C_2H_2 gas (or a mixture of SiH_4 to C_2H_2 was ~8:1) was fed in for AGNR growth and the pressure was kept at ~1.6 (~5.2) Pa. During heating, annealing and cooling, the pressure was kept at ~7 Pa with an Ar flow of 10 sccm for all samples.

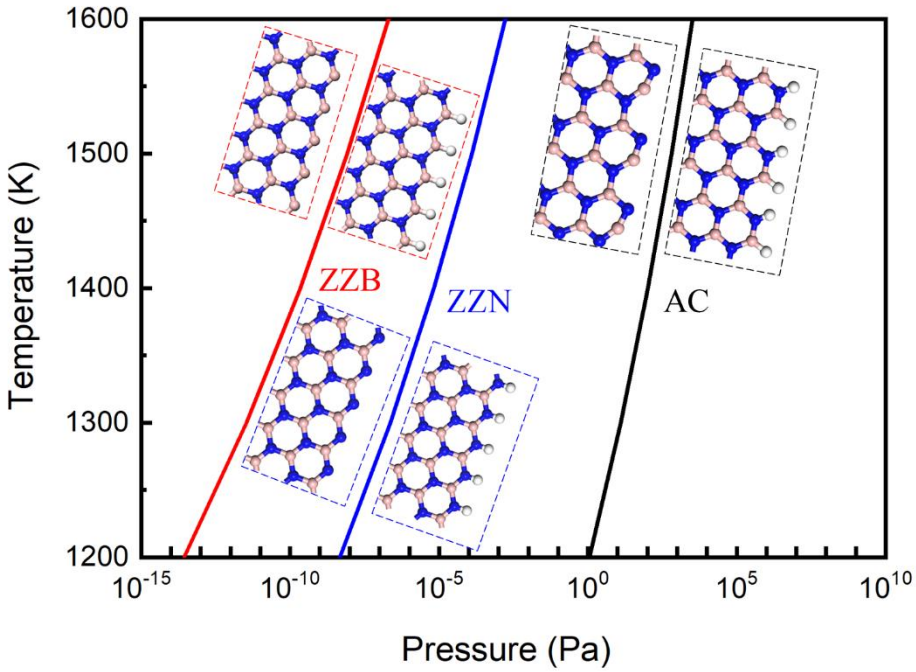

Fig. S4. Thermodynamic diagrams of *h*-BN edges with configurations of zigzag boron (ZZB), zigzag nitrogen (ZZN) and armchair (AC). The edge structure of *h*-BN is highly dependent on the temperature and hydrogen pressure. Edges at the left side of the phase transition line are non-passivated while edges at the right side of line is hydrogen passivated. ZZB edge is easily to be passivated even at very low hydrogen pressure. AC edge is very stable and only very high hydrogen pressure can passivate it.

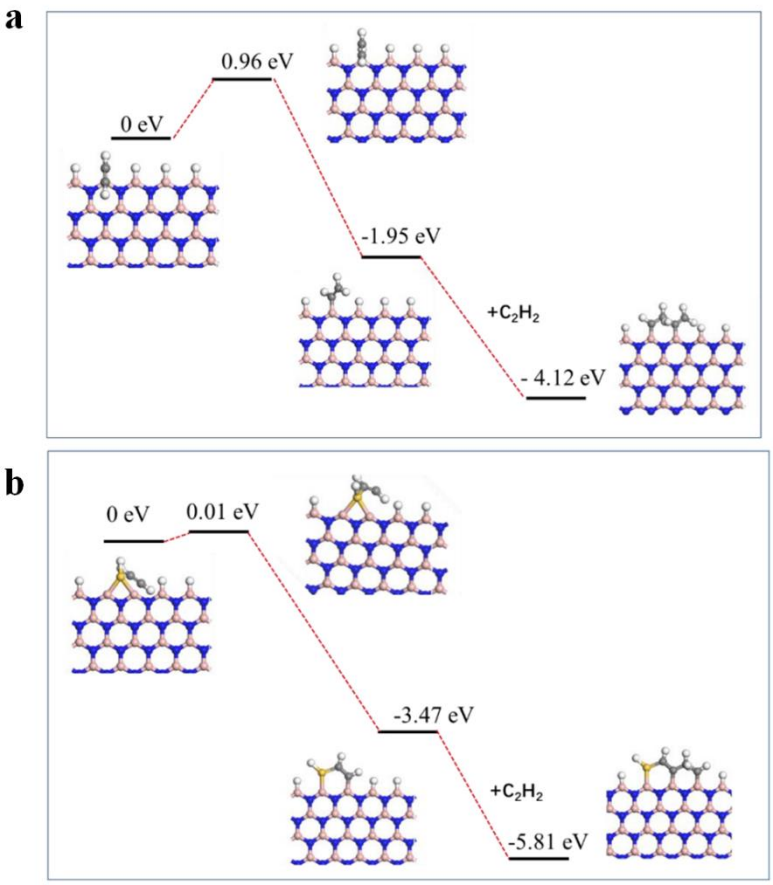

Fig. S5. Energy profiles for the growth of GNR at ZZB edge without and with the catalyst of silane. (a) GNR growth on H-passivated ZZB edge of *h*-BN. **(b)** GNR growth at the H-passivated ZZB edge of *h*-BN by using silane as a catalyst. The using of silane catalyst greatly decreases the activation barrier of C_2H_2 incorporation into the edge.

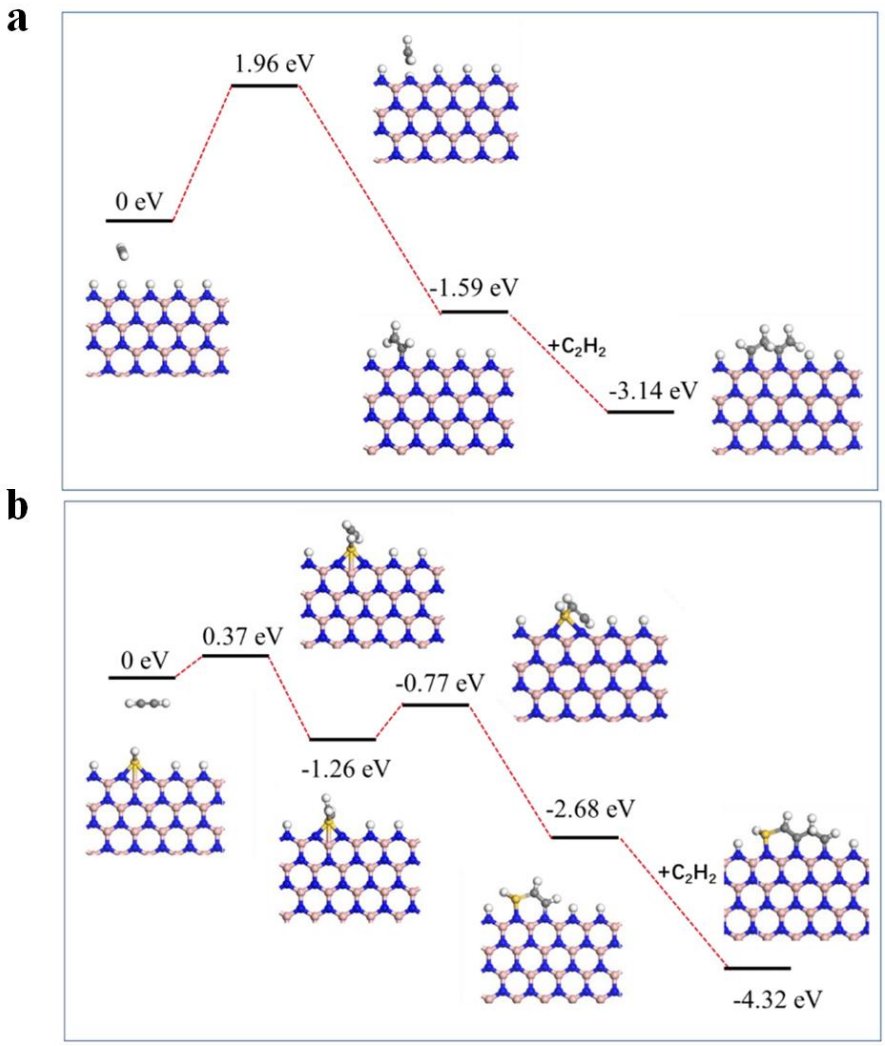

Fig. S6. Energy profiles for the growth of GNR at ZZN edge without and with the catalyst of silane. (a) GNR growth on H-passivated ZZN edge of *h*-BN. **(b)** GNR growth at the H-passivated ZZ edge of *h*-BN by using silane as a catalyst. The using of silane catalyst greatly decreases the activation barrier of C_2H_2 incorporation into the edge.

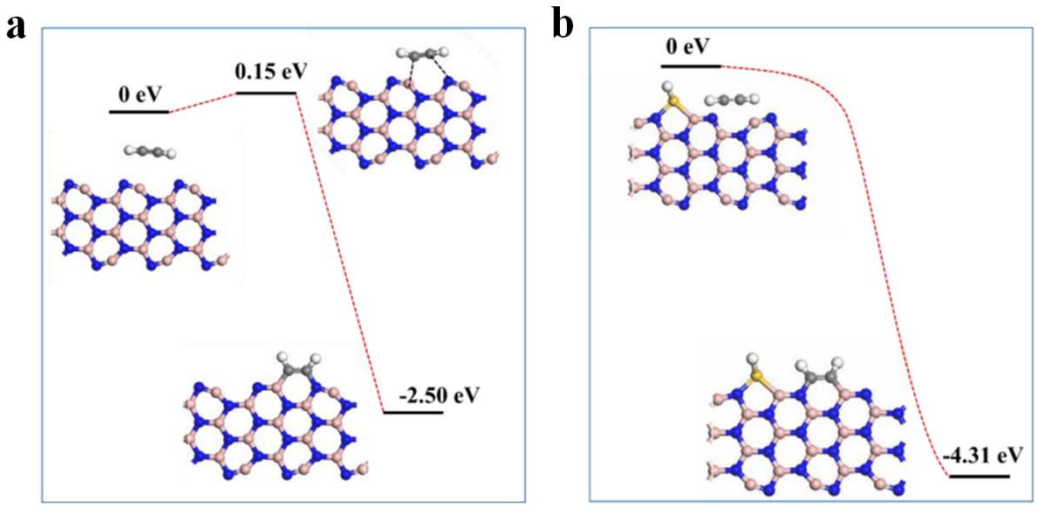

Fig. S7. Energy profiles for the growth of GNR at AC edge without and with the catalyst of silane. (a) GNR growth at the AC edge of *h*-BN. **(b)** GNR growth at the AC edge of *h*-BN by using silane as a catalyst. Both edges have very low activation barrier to the addition of C_2H_2.

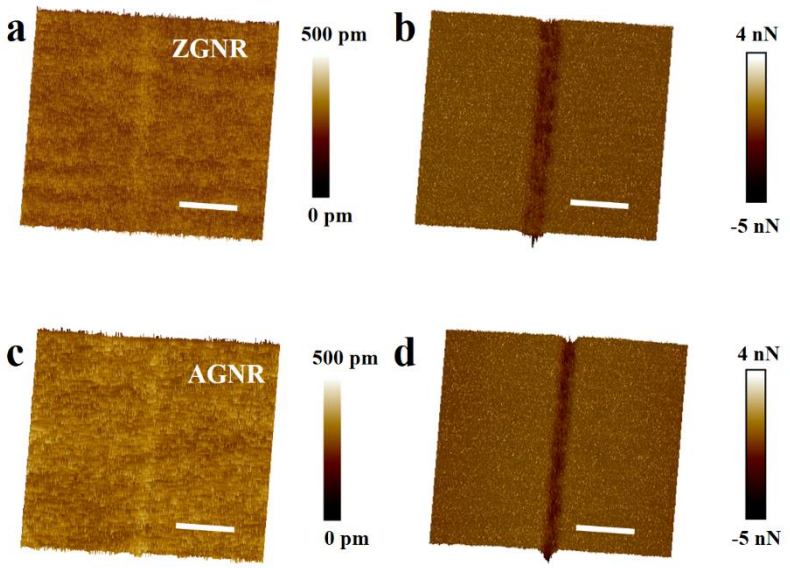

Fig. S8. AFM images of ultra-narrow GNRs embedded within *h*-BN substrate. (a) 3D AFM height image and **(b)** 3D friction image of a sub-5 nm-wide ZGNR on an *h*-BN substrate. **(c)** 3D AFM height image and **(d)** 3D friction image of a sub-5 nm-wide AGNR in an *h*-BN substrate. The scale bars are 20 nm.

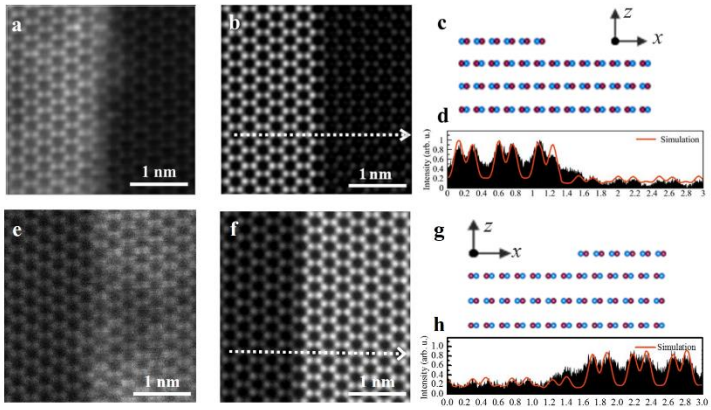

Fig. S9. Atomic resolution analysis on the zigzag edge of *h*-BN trench. (a,e) Wiener filtered HAADF-STEM images of *h*-BN edge. **(b,f)** Simulated HAADF images of the models corresponding the experimental images. **(c,g)** Top views of the rigid models showing the etched trench of *h*-BN crystal consisting of 4 layers. In the model, blue and red correspond to Nitrogen and Boron, respectively. **(d,h)** Intensity profiles recorded over the dashed line on panel b and f, respectively.

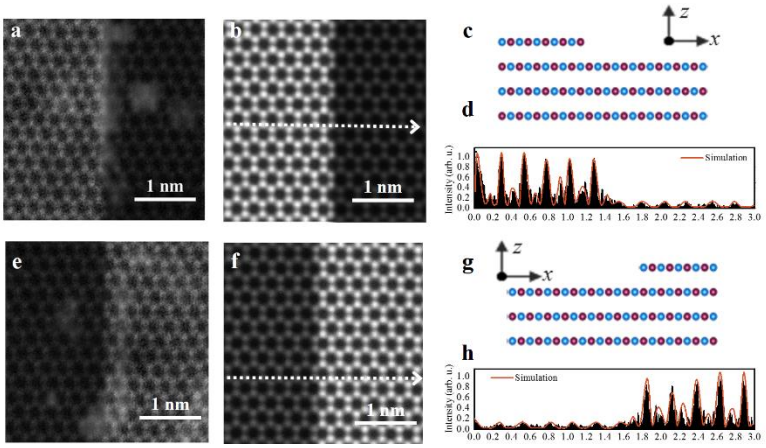

Fig. S10. Atomic resolution analysis on the armchair edge of *h*-BN trench. (a,e) Wiener filtered HAADF-STEM images of *h*-BN edge. **(b,f)** Simulated HAADF images of the models corresponding the experimental images. **(c,g)** Top views of the rigid models showing the etched trench of *h*-BN crystal consisting of 4 layers. In the model, blue and red correspond to Nitrogen and Boron, respectively. **(d,h)** Intensity profiles recorded over the dashed line on panel b and f, respectively.

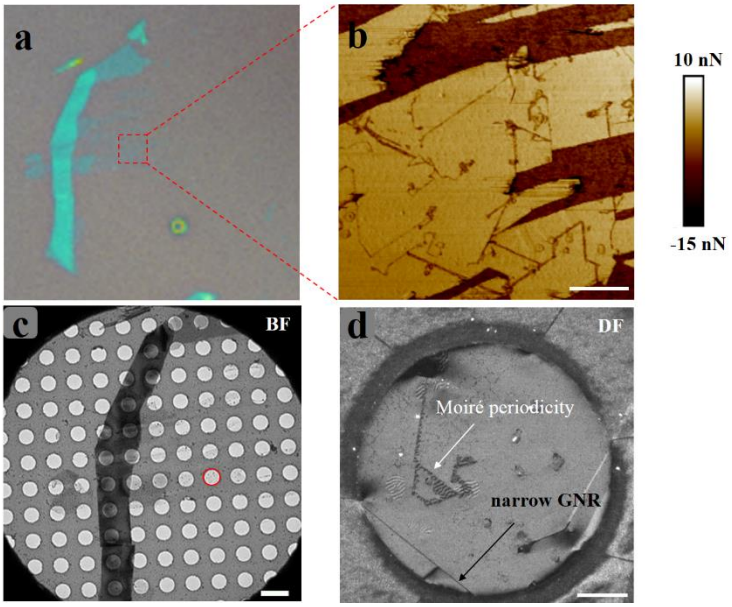

Fig. S11. TEM sample preparation and characterization of GNRs embedded in *h*-BN. (a) Optical image of *h*-BN flakes exfoliated on a Si substrate with 300 nm SiO_2. **(b)** The AFM friction image taken in the area of the red dashed frame shown in (a), scale bar 600 nm. The dark stripes are GNRs. The thickness of the thin *h*-BN flake is in the range of 1.3-2.2 nm, which corresponds to 3-5 layers of *h*-BN. **(c)** TEM bright field (BF) image of the sample shown in (a) after being transferred onto a TEM grid. The scale bar is 3 μm. **(d)** TEM dark field (DF) image of the region inside the red circle in (c). The black arrow points to a narrow GNR. The white arrow points to a ~14 nm Moiré periodicity, which corresponds to the lattice mismatch between graphene and *h*-BN. The scale bar is 200 nm.

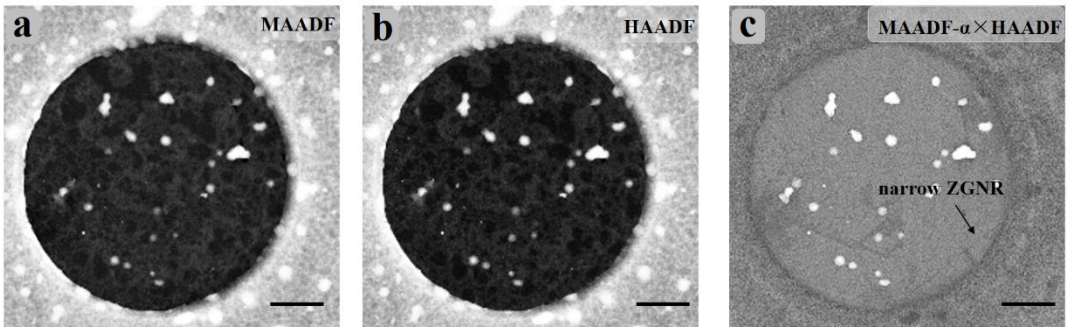

Fig. S12. The STEM images of GNR. (a) Medium angle annular dark field (MAADF). **(b)** High angle annular dark field (HAADF). **(c)** MAADF-α×HAADF images, α is a variable value which is adjusted so as to minimize the contrast of adsorbed contamination. The arrow points to the narrow ZGNR corresponding to the same ZGNR shown in **Extended Data Fig.** 2i-k and **Fig.** S11d. The scale bars are 200 nm.

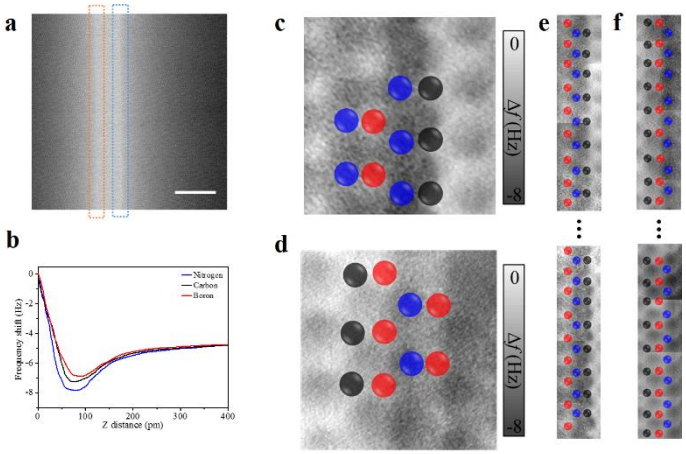

Fig. S13. High-resolution AFM investigation on ZGNR. (a) A typical nc-AFM image of a ZGNR embedded in *h*-BN in constant-height mode. Scale bar: 4 nm. **(b)** Force spectroscopies taken at different elements in the embedded ZGNR. (c) A zoom-in view of one boundary of ZGNR-*h*-BN, here boron in red, carbon in black and nitride in blue. **(d)** A close view of the other edge of ZGNR-*h*-BN. **(e-f)** A series of nc-AFM images which were continuously measured along the opposite boundaries in the orange (nitride terminated) and blue (boron terminated) box indicated in (a), respectively. The nc-AFM measurement parameters: V_{tip} = 0 mV while the amplitude was kept at ~60 pm.

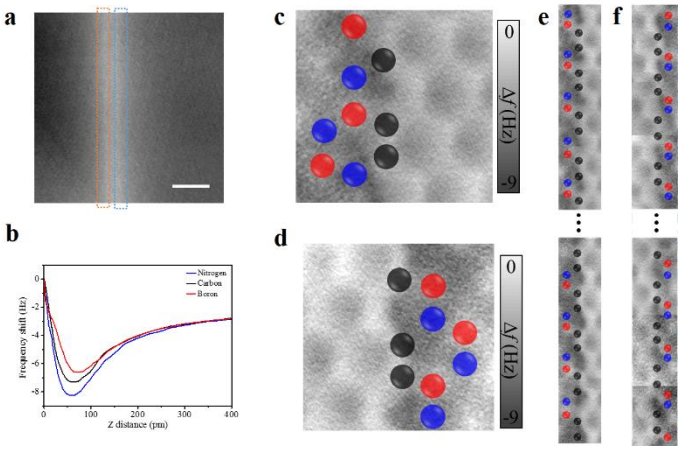

Fig. S14. High-resolution AFM results of AGNR. (a) A typical constant-height nc-AFM image of an AGNR embedded in *h*-BN. Scale bar: 10 nm. **(b)** Force spectroscopies taken at different elements in the embedded AGNR. **(c-d)** Zoom-in views of the boundaries of AGNR-*h*-BN with boron in red, carbon in black and nitride in blue. **(e-f)** A series of nc-AFM images corresponding to orange and blue box in (a). The parameters for nc-AFM measurement: V_{tip} = 0 mV while the amplitude was kept at ~60 pm.

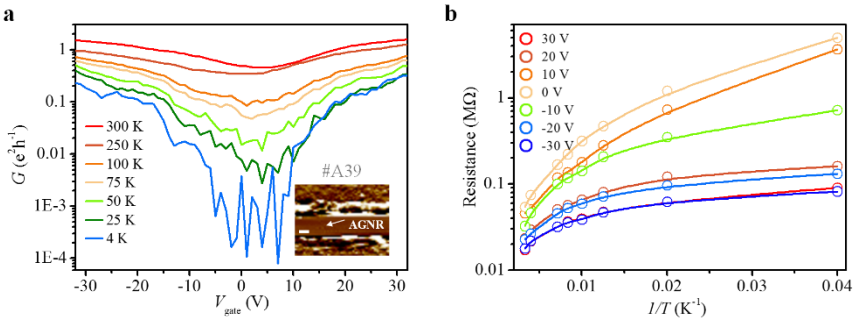

Fig. S15. Electronic transport through a sub-5 nm AGNR device on *h*-BN. (a) Conductance (G) of an armchair graphene nanoribbon (AGNR) with a width of ~5 nm as a function of back gate voltage (V_{gate}). The inset shows an AFM friction image of the AGNR channel corresponding to the transfer curves. The scale bar is 200 nm. The channel length is about 278 nm. Its field effect mobility is about 1,700 $cm^2V^{-1}s^{-1}$ at 300 K. **(b)** Resistance (R) under different V_{gate} versus temperature (T) from 25 to 300 K for the 5 nm-wide AGNR, the solid curves are fits based on a simple two-band model, the extracted band gap is about 183.2±18.7 meV.

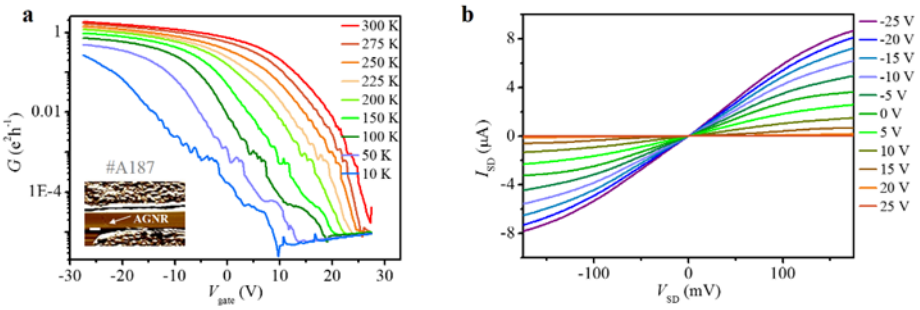

Fig. S16. Electronic transport through a sub-5 nm AGNR device on *h*-BN. (a) Conductance (G) of an armchair graphene nanoribbon (AGNR) with an estimated width of about 4.8 nm. The conductance can be completely switched off even at room temperature. The inset shows the AFM friction image of the nanoribbon channel corresponding to the transfer curves. The scale bar in the inset is 200 nm. Its field effect mobility is about 1,428 $cm^2V^{-1}s^{-1}$ at 300 K. The GNR field effect transistor (FET) in a channel length of about 236 nm exhibits rather high $G = 1.8\ e^2h^{-1}$ at room temperature when $V_{gate} = -25$ V. Charge carrier was scattered for $(4e^2h^{-1})/(1.8\ e^2h^{-1}) \approx 2$ times. The scattering mean free path (MFP) is estimated to be about 236 nm/(2+1) = 79 nm even without excluding the contribution from the contact. The extracted band gap by STB model is 530.9±34.7 meV. **(b)** I_{SD}-V_{SD} curves for the device in (a) at different gate bias voltages at room temperature.

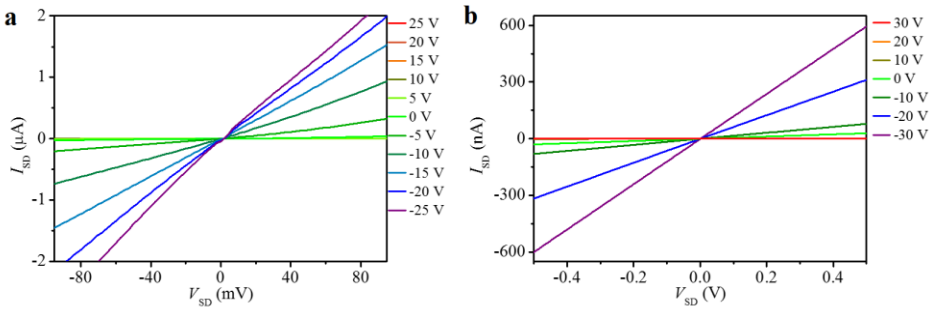

Fig. S17. I_{SD}-V_{SD} characteristics recorded under different V_{gate} when **(a)** T = 100 K for the device shown in **Fig.** S16 and **(b)** T = 150 K for the device shown in **Fig.** S15.

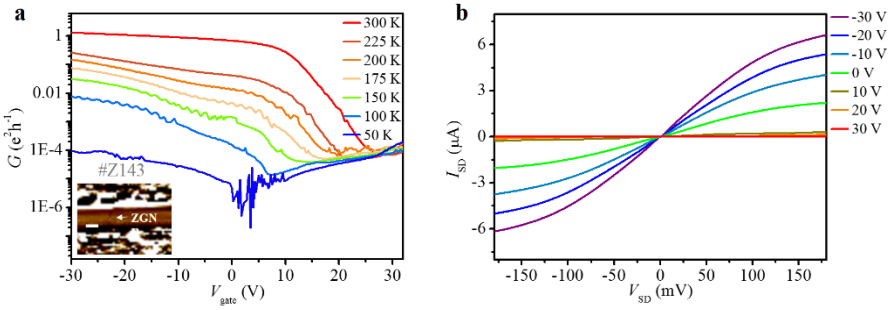

Fig. S18. Electronic transport through a sub-5 nm ZGNR device on *h*-BN. (a) Gate voltage dependence of the conductance (G) of a ZGNR with an estimated width of about 5 nm. The conductance can be switched off even at room temperature. The inset shows an AFM friction image of the nanoribbon channel corresponding to the transfer curves. The channel length is about 247 nm. The scale bar in the inset is 200 nm. Its field effect mobility is about 1,639 $cm^2V^{-1}s^{-1}$ at 300 K. The GNR field effect transistor (FET) with a channel length of about 247 nm exhibits a rather high $G = 1.3\ e^2h^{-1}$ at room temperature when V_{gate}= -30 V. Charge carrier was scattered for $(4\ e^2h^{-1})/(1.3\ e^2h^{-1}) \approx 3$ times. The scattering mean free path (MFP) is estimated to be about 247 nm/(3+1) = 62 nm even without excluding the contribution from the contact. The extracted band gap by STB model is 436.2±28.1 meV. **(b)** I_{SD}-V_{SD} curves for the same device in (a) at different gate bias voltages at room temperature.

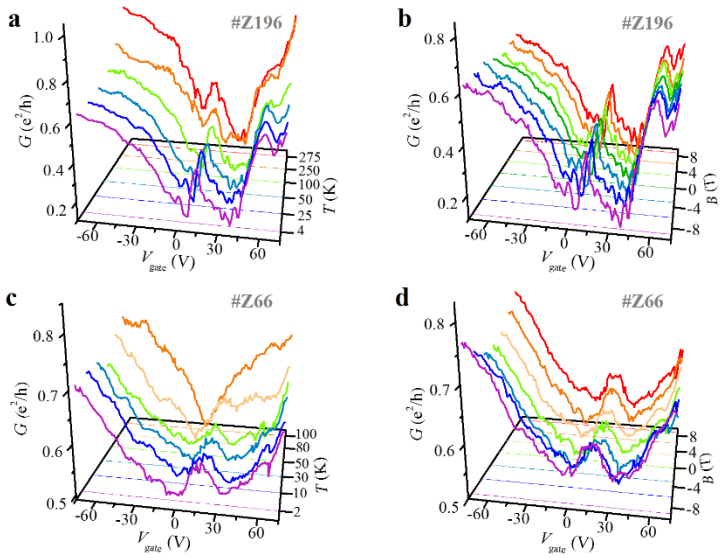

Fig. S19. The influence of magnetic field and temperature on transport properties of ZGNRs. Transfer curves of **(a)** sample #Z196 and **(c)** sample #Z66 at different temperatures. **(b)** Transfer curves for sample #Z196 subjected to different magnetic field (*B*) at the temperature of 4 K. **(d)** The typical transfer curves for sample #Z66 at several *B* at 2 K. All the measurements were under V_{SD} = 20 mV.

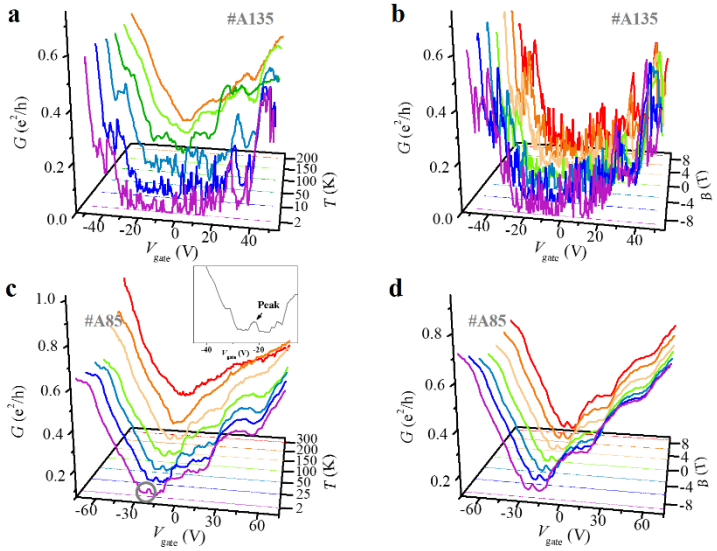

Fig. S20. **The influence of magnetic field and temperature on transport properties of AGNRs.** The typical transfer curves for **(a)** sample #A135 and **(c)** sample #A85 at several temperatures. The inset shows enlarged area in the grey circle in (c). The typical transfer curves for **(b)** sample #A135 and **(d)** sample #A85 at several *B* at 2 K. All the measurements were under V_{SD} = 10 mV.

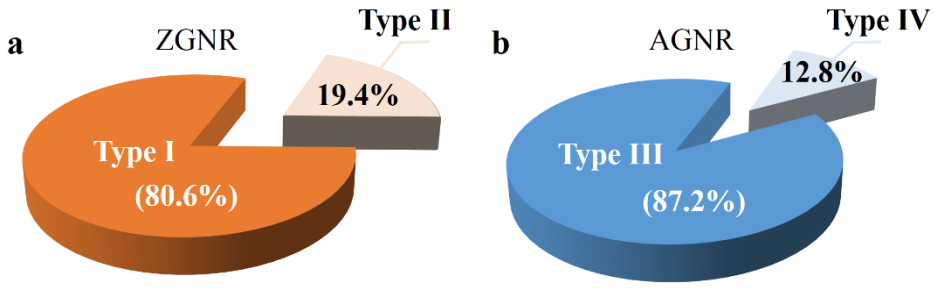

Fig. S21. The investigation on conductance peak in GNRs. (a) Pie chart of distribution of different ZGNRs. Type I corresponds to ZGNRs whose peaks always exist even at high temperature (a typical example: #Z196), and Type II represents ZGNRs whose peaks disappear at high temperature (a typical example: #Z66). **(b)** Pie chart of distribution of different AGNRs. Type III is AGNR whose transfer curves are in absence of nontrivial conductance peaks at any temperature (a typical example: #A135) and Type IV means AGNR whose transfer curve is of a tiny peak at low temperature (a typical example: #A85).

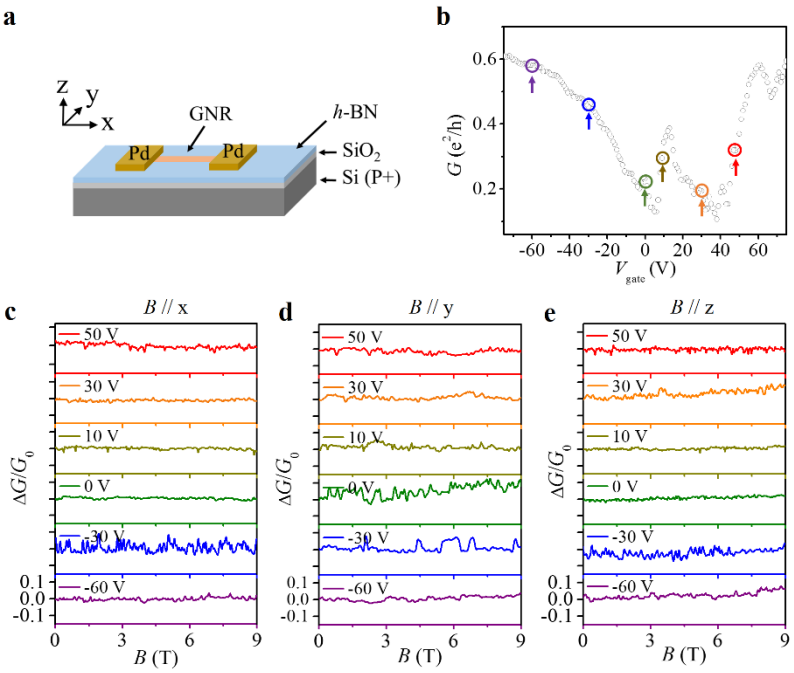

Fig. S22. Magneto-electronic properties of a typical Type I ZGNR FET (sample #Z196) under different V_{gate}. (a) Schematic of a ZGNR device. **(b)** Transfer characteristics of the 8.9 ± 0.5 nm ZGNR FET. **(c-e)** Normalized MC measured at selected V_{gate} indicated by the colored dots marked on the transfer curve shown in (a), the magnetic field was applied (c) in parallel with the direction of the current, (d) in the plane of the substrate, but perpendicular to the current, and (e) perpendicular to the substrate plane. All the measurements were carried out at 4 K with V_{SD} = 20 mV.

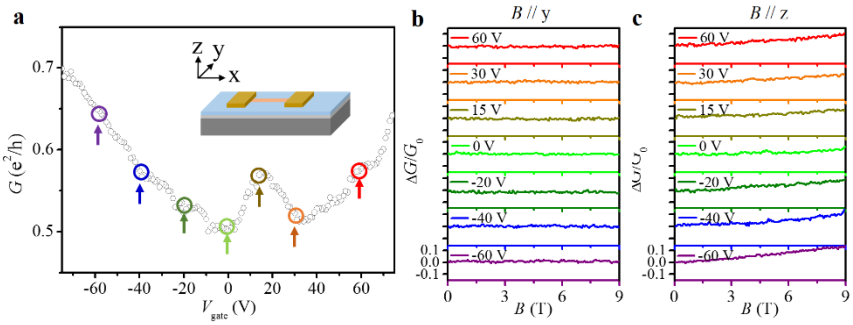

Fig. S23. Magneto-electronic properties of a typical Type II ZGNR FET (sample #Z66). (a) Transfer characteristics for the 9.2 ± 0.5 nm ZGNR with Pd contacts. Inset: Schematic of the ZGNR device. Normalized MC measured at different V_{gate} indicated by the colored dots marked on the transfer curve in (a) when the magnetic field was applied **(b)** in the plane of the substrate but perpendicular to the current, or **(c)** perpendicular to the substrate. All the measurements were carried out when V_{SD} = 20 mV and T = 2 K.

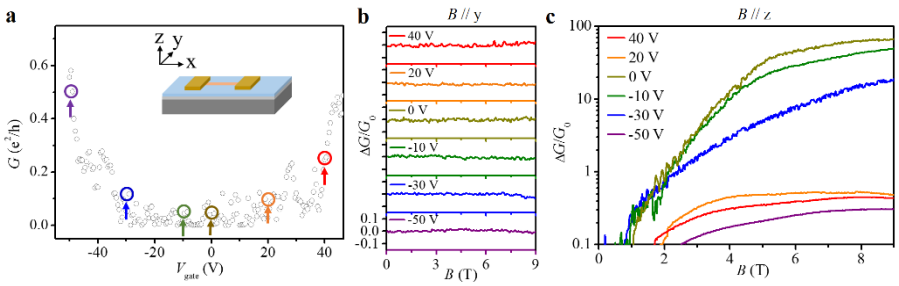

Fig. S24. Magneto-electronic properties of Type III AGNR FET (sample #A135). (a) Transfer characteristics for the 9.5 ± 0.5 nm AGNR FET, colored circles (and the arrows) denote certain V_{gate} where magneto-conductance (MC) was measured; Normalized magneto-conductance measured at selected V_{gate}, when **(b)** *B*//y and **(c)** *B*//z. All the measurements were carried out under V_{SD} = 10 mV at 2 K.

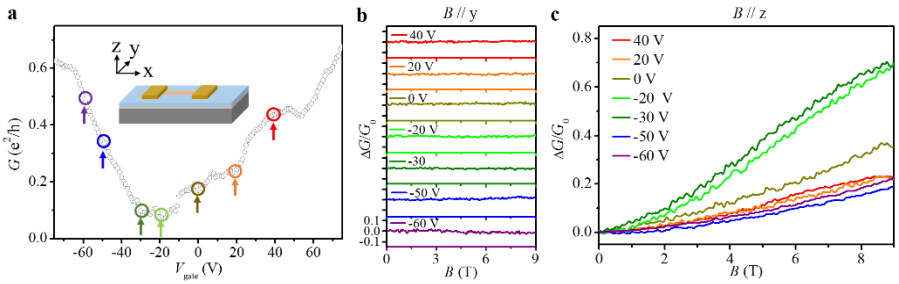

Fig. S25. Magneto-transport in Type IV AGNR (sample #A85). (a) Transfer characteristic for the 8.7 ± 0.5 nm AGNR; Normalized MC measured at different V_{gate} indicated by the colored dots marked on the transfer curve shown in (a), when **(b)** *B*//y and **(c)** *B*//z. All the measurements were under V_{SD} = 10 mV at 2 K.

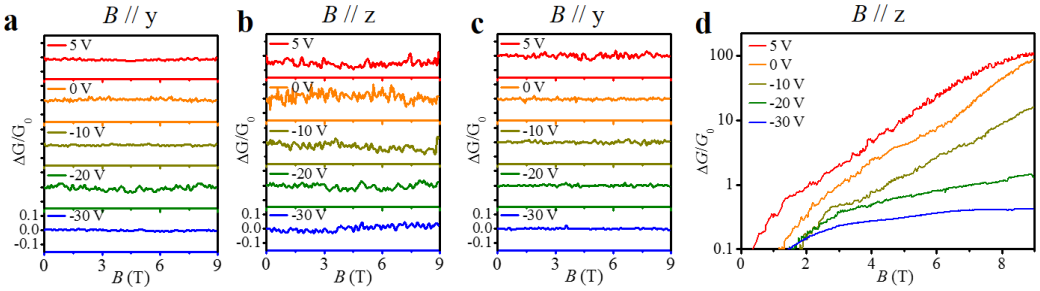

Fig. S26. Magneto-electronic properties of GNR FETs under different V_{gate}. (a-b) Normalized MC for a 5 nm-wide ZGNR (sample #Z143) measured at selected V_{gate}, (a) *B*//y and (b) *B*//z. All the measurements were carried out at 4 K with V_{SD} = 20 mV. **(c-d)** Normalized MC for a 4.8 nm-wide AGNR (sample #A187) measured at different V_{gate}, when (c) *B*//y and (d) *B*//z. All the measurements were carried out at 2 K with V_{SD} = 10 mV.

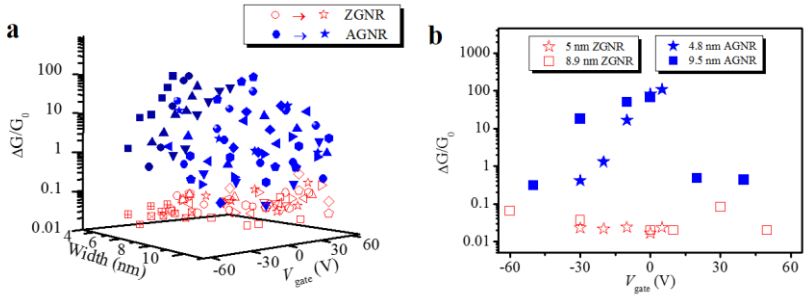

Fig. S27. Distribution of MC of all GNRs measured. (a) Normalized magneto-conductance as a function of V_{gate} for GNR in different width subjected to a magnetic field of 9 T perpendicular to the substrate. The red open symbols represent the normalized MC for ZGNR samples and the blue solid symbols represent AGNR samples. **(b)** Value of normalized MC as a function of V_{gate} for typical GNRs with some typical width subjected a magnetic field of 9 T perpendicular to the substrate for 5 nm-wide ZGNR (sample #Z143), 8.9 nm-wide ZGNR (sample #Z196), 4.8 nm-wide AGNR (sample #A187) and 9.5 nm-wide AGNR (sample #A135), respectively.

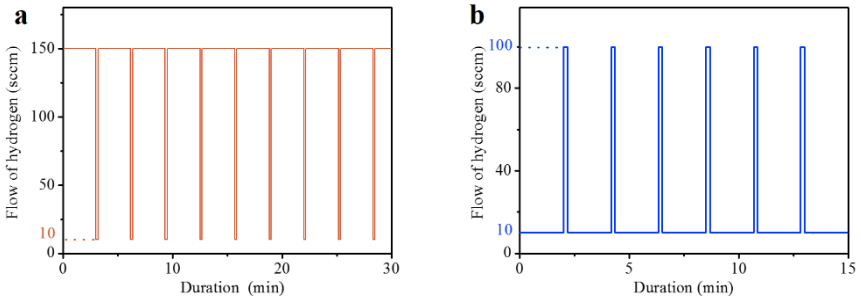

Fig. S28. Schematic diagrams of typical processes for etching nanotrenches on *h*-BN to shorten the smooth segments. (a) A typical etching process for ZZ-oriented trenches. The $NiCl_2$-coated samples were annealing at 1,200 °C for 30 min under a 10 s outage of hydrogen flow 150/10 sccm every 3 min. **(b)** A typical etching process for AC-oriented trenches. The H_2PtCl_6-coated samples were annealed at 1,300 °C for 15 min under a 10 s pulse of hydrogen flow 10/100 sccm every 2 min.

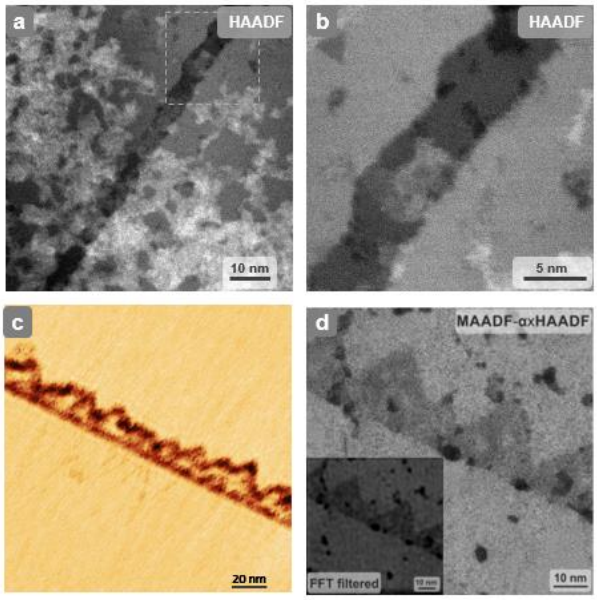

Fig. S29. High resolution analysis of the imperfect parts of edge-specific GNRs with short smooth segments. **(a)** A STEM HAADF image for an imperfect part of an AGNR_SS sample. **(b)** A zoomed-in view of the region in the white dashed box shown in **a**. **(c)** An AFM friction image for an imperfect part of a ZGNR_SS sample. **(d)** A STEM MAADF-α×HAADF image for the imperfect part of another ZGNR_SS sample, inset shows the FFT filtered image.

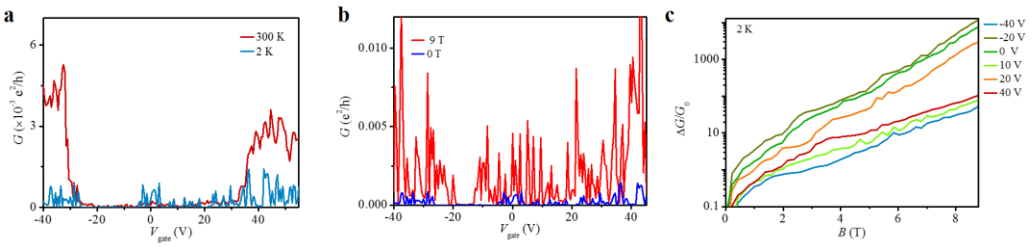

Fig. S30. Electrical transport properties of a FET made from sub-5 nm wide ZGNR with short smooth segments. Its channel length l is ~240 nm. **(a)** G-V_{gate} characteristics of the GNR device under 300 and 2 K. **(b)** G-V_{gate} characteristics of the device subjected to different magnetic fields (B) at the temperature of 2 K. **(c)** Normalized magnetic conductance (MC) measured at different V_{gate}. All the measurements were under V_{SD} = 20 mV.

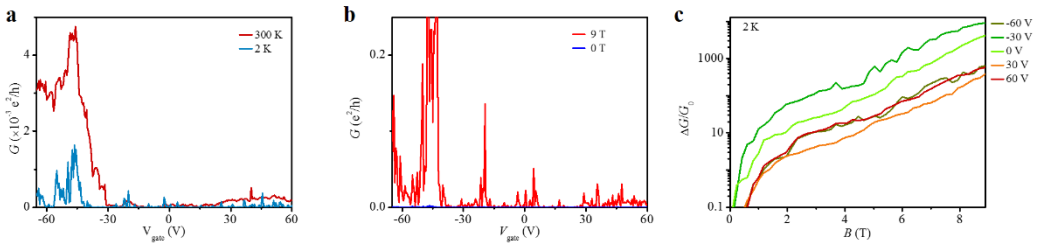

Fig. S31. Electrical transport properties of a FET made from sub-5 nm AGNR with short smooth segments. **(a)** Transfer characteristics of the GNR device under 300 and 2 K. **(b)** Transfer curves for the device subjected to different B at the temperature of 2 K. **(c)** Normalized MC measured at different V_{gate}. All the measurements were under V_{SD} = 20 mV.

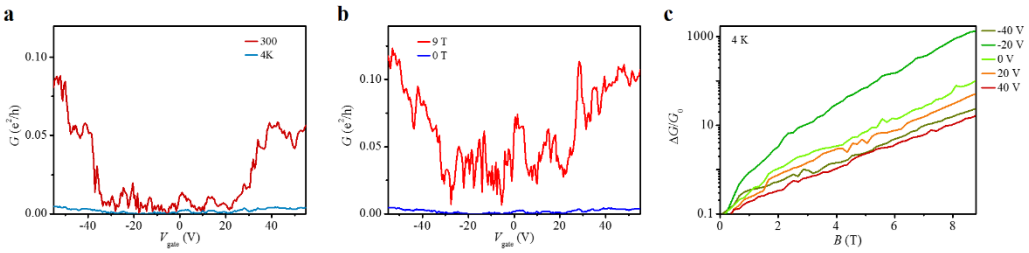

Fig. S32. Electronic transport properties of a FET made from ~10 nm ZGNR with short segments in smooth edges. (a) Transfer curves of the GNR device under 300 and 4 K. **(b)** Transfer curves for the device subjected to different B at 4 K. **(c)** Normalized MC measured at different V_{gate}. All the measurements were carried out under V_{SD} = 20 mV.

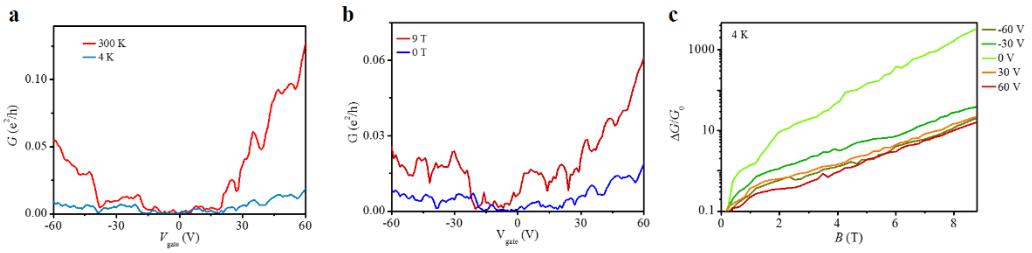

Fig. S33. Electronic transport properties of a FET made from ~10 nm AGNR with short smooth segments. **(a)** Transfer curves of the GNR device under 300 and 4 K. **(b)** Transfer curves for the device subjected to different B at 4 K. **(c)** Normalized MC measured at different V_{gate}. All the measurements were under V_{SD} = 20 mV.

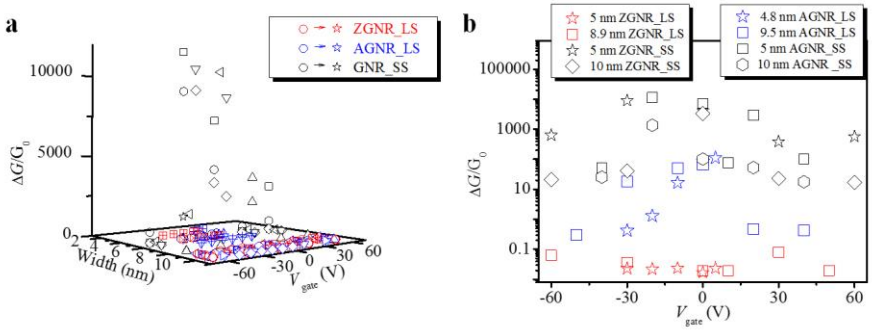

Fig. S34. Distribution of MC of all GNRs measured. (a) Normalized MC as a function of V_{gate} for GNR in different widths subjected to a magnetic field of 9 T perpendicular to the substrate. The red open symbols represent the normalized MC for ZGNR with long smooth segments (ZGNR_LS) samples, the blue solid symbols represent AGNR with long smooth segments (AGNR_LS) samples and the black open symbols represent GNRs with short smooth segments (GNR_SS). **(b)** Value of normalized MC as a function of V_{gate} for typical GNRs with some typical width subjected a magnetic field of 9 T perpendicular to the substrate for 5 nm-wide ZGNR_LS (sample #Z143), 8.9 nm-wide ZGNR_LS (sample #Z196), 5 nm-wide ZGNR_SS (sample #SSZ002), 10 nm-wide ZGNR_SS (sample #SSZ023), 4.8 nm-wide AGNR_LS (sample #A187) and 9.5 nm-wide AGNR_LS (sample #A135), 5 nm-wide AGNR_SS(sample #SSA012), and 10 nm-wide AGNR_SS(sample #SSA022), respectively.

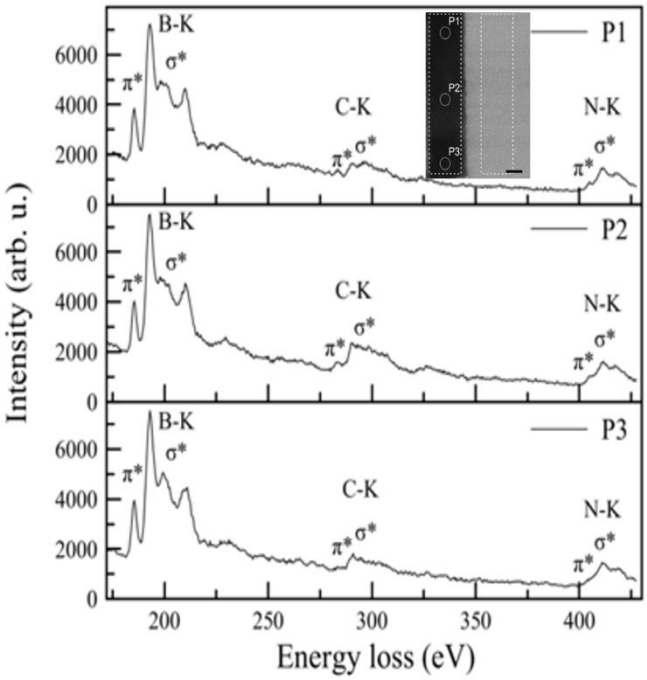

Fig. S35. EELS measurement on ZGNR embedded in *h*-BN. Inset shows the STEM-MAADF image of a ZGNR with the width ~5 nm, the scale bar is 3 nm. EELS spectrum recorded over the areas shown in the left dashed circles region (P1, P2, P3) in the inset.

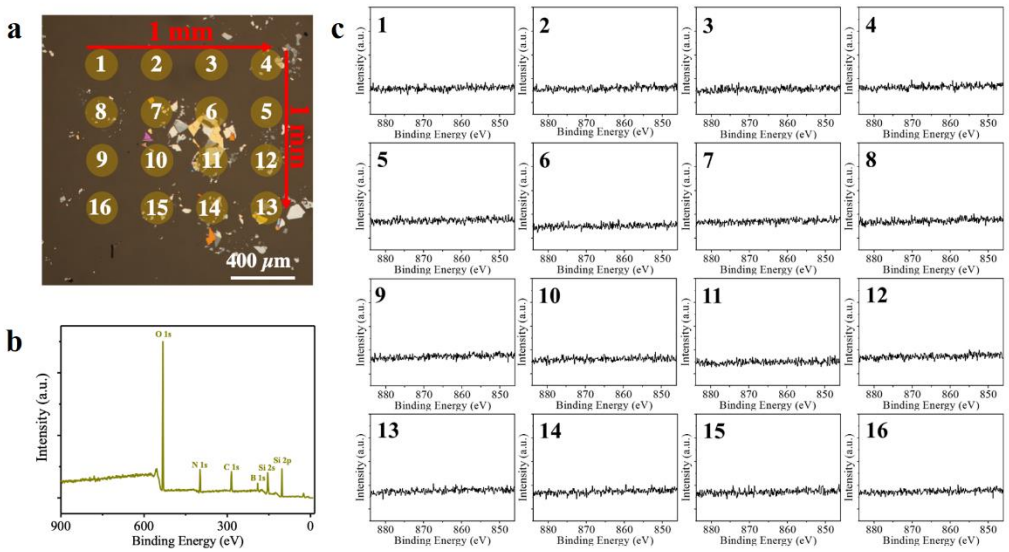

Fig. S36. XPS analysis of embedded ZGNRs in *h*-BN flakes on quartz substrate after growth. (a) Optical image of ZGNR/*h*-BN on quartz substrate. The XPS mapping area is 1 ×1 mm^2. **(b)** XPS survey spectrum of embedded ZGNR in *h*-BN flakes at position 11. The B 1s and N 1s signals are detectable. **(c)** Ni 2p spectra of embedded ZGNR in *h*-BN flakes randomly taken from 16 locations on the quartz substrate. The Ni signal is not detectable.

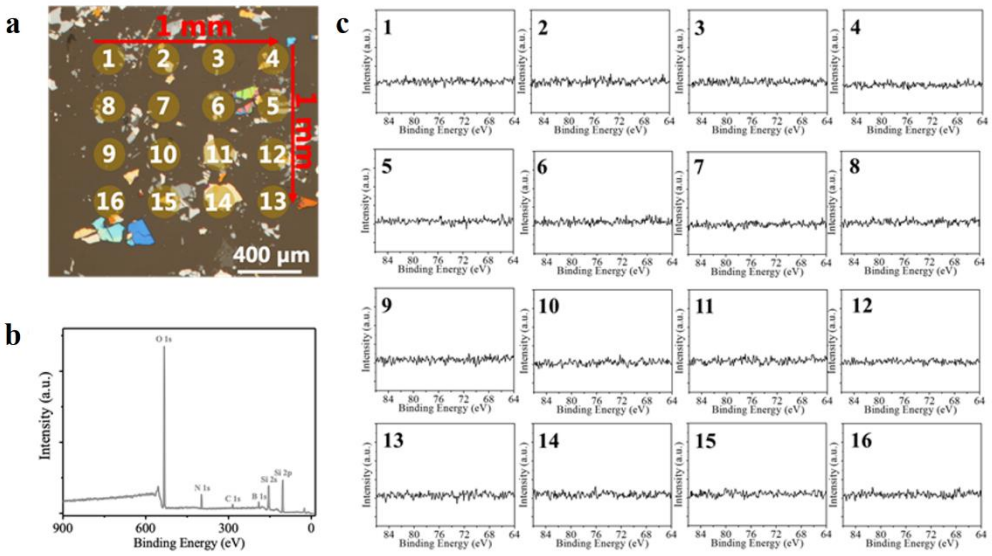

Fig. S37. XPS analysis of embedded AGNRs in *h*-BN flakes on quartz substrate. (a) Optical image of AGNR/*h*-BN on quartz substrate. **(b)** XPS survey spectrum of embedded AGNR in *h*-BN flakes at position 14. The B 1s and N 1s peaks are visible. **(c)** Pt 4f spectra of embedded AGNR in *h*-BN flakes taken from 16 locations on the quartz substrate. The Pt4f signal is not detected.

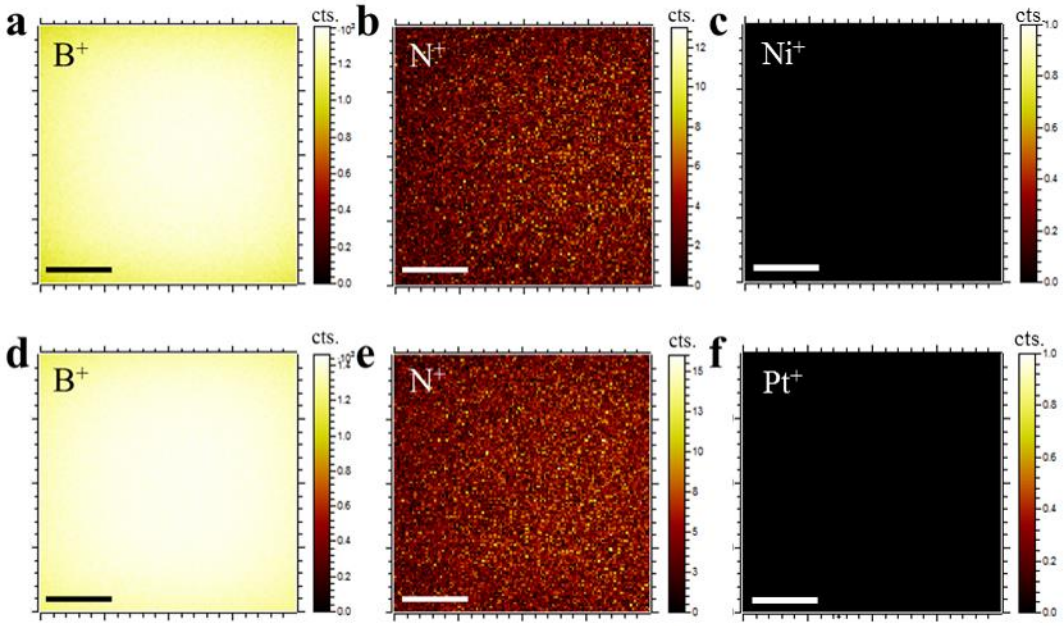

Fig. S38. Planar distribution of the main elements on GNR sample. (a-c) TOF-SIMS maps of B+, N+, and Ni+ secondary ions after the growth of ZGNR, respectively. The Ni+ signal corresponds to the nickel nanoparticles. **(d-f)** TOF-SIMS maps of B+, N+, and Pt+ secondary ions on an AGNR sample, respectively. The low Pt+ secondary ion signal indicates that the concentration of platinum nanoparticles after growth is too low to detect. Scale bars, 10 μm.

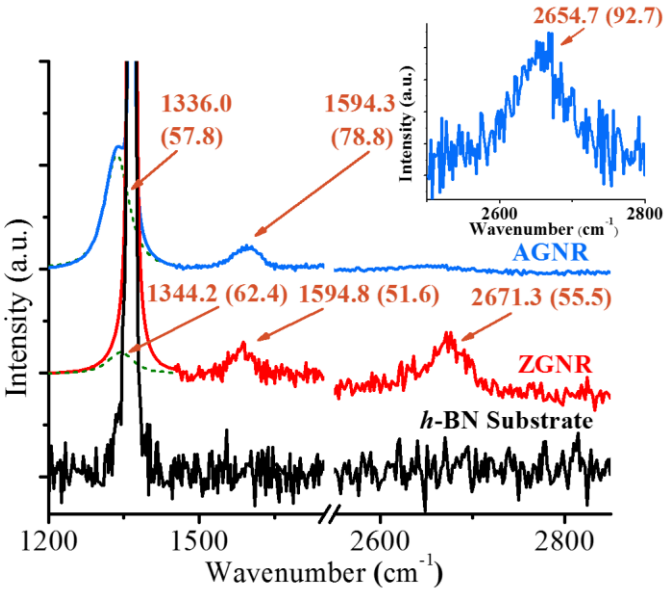

Fig. S39. Raman scattering of a ZGNR and an AGNR on *h*-BN. The Raman spectrum of *h*-BN is also shown beside those of the GNRs for comparison. The spectrum traces were normalized and shifted on the intensity axis for clarity. The inset shows a zoomed-in view of the 2D peak of AGNR. The fitted D peak (green) is extracted from the measured spectra because the position of the D-band of the GNRs is very close to that of a prominent Raman peak of *h*-BN. The full width at half-maximum (FWHM) for each peak is given in parentheses with the peak position.

Supplementary Tables

Experiment	Atmosphere	Temperature (°C)	$NiCl_2$ solution concentration (g/L)	Etching duration (min)	Length (μm)	Width (nm)	Aspect ratio
#1	Ar:H_2= 9:1 150 Pa	1100	0.1	180	N.A.	N.A.	N.A.
#2	Ar:H_2= 9:1 150 Pa	1150	0.1	60	N.A.	N.A.	N.A.
#3	Ar:H_2= 9:1 150 Pa	1150	0.1	180	~0.5	<10	~50
#4	Ar:H_2= 9:1 150 Pa	1200	0.1	30	~1	<5	>200
#5	Ar:H_2= 9:1 150 Pa	1200	0.1	60	~1.5	<10	>150
#6	Ar:H_2= 9:1 150 Pa	1200	0.1	180	~2	~10	~200
#7	Ar:H_2= 9:1 150 Pa	1250	0.1	15	~1	~5	~200
#8	Ar:H_2= 9:1 150 Pa	1250	0.1	30	~1.5	~10	~150
#9	Ar:H_2= 9:1 150 Pa	1300	0.1	15	~1.5	~15	~100
#10	Ar:H_2= 9:1 150 Pa	1300	0.1	30	~1	~20	~50

Table S1. Summary of nickel-particle-assisted etching experiments under different conditions. Both the length and width of the *h*-BN trenches exhibit dependence on the experimental conditions, such as the pressure of the carrying gases, temperature, the concentration of the $NiCl_2$ solution, and the etching duration. The width of the trenches most strongly depends on the etching temperature and the duration. The dependent relationship makes sense as etching is normally based on a thermally activated reaction. In the experiment, we focus on fabrication of narrow trenches (sub-5 nm), so the etching atmosphere and $NiCl_2$ solution concentration were optimized and fixed. Compared to the length, the width of trenches is more sensitive to temperature and etching duration, while the evolution of the length and the width does not seem to follow the well-known Arrhenius law, most likely due to the involvement of additional etching mechanisms, for example, hydrogen-activated etching.

Experiment	Atmosphere	Temperature (°C)	H_2PtCl_6 concentration (ml/L)	Etching duration (min)	Length (μm)	Width (nm)	Aspect ratio
#1	Ar:H_2= 3:1 10 Pa	1150	10	180	N.A.	N.A.	N.A.
#2	Ar:H_2= 3:1 10 Pa	1200	10	60	~0.5	~10	~50
#3	Ar:H_2= 3:1 10 Pa	1200	10	180	~1	~20	~50
#4	Ar:H_2= 3:1 10 Pa	1250	10	30	~1	~10	~100
#5	Ar:H_2= 3:1 10 Pa	1250	10	60	~1.5	~20	~75
#6	Ar:H_2= 3:1 10 Pa	1250	10	180	~2.5	~30	~80
#7	Ar:H_2= 3:1 10 Pa	1300	10	15	~2	<5	>400
#8	Ar:H_2= 3:1 10 Pa	1300	10	30	~2.5	~15	~160
#9	Ar:H_2= 3:1 10 Pa	1350	10	15	~1.5	~10	~150
#10	Ar:H_2= 3:1 10 Pa	1350	10	30	~1	~20	~50

Table S2. Summary of platinum-particle-assisted etching experiments under different condition. Similar to the nickel-assisted-etching, both the length and width of the *h*-BN nano-trenches exhibit an obvious dependence on the experimental parameters. Compared to the ZZ oriented etching, the AC trenches are more sensitive to temperature and much easier to broaden.

Supplementary Text

Discussion on mechanism for selective etching of *h*-BN nano-trenches

The nanoparticle catalytic etching plays very important roles in determining the orientation and width of nano-trenches, and finally those of GNRs in *h*-BN. The mechanism behind this is worth discussing. Our experiments show that the anisotropic cutting and etching of *h*-BN sheets depend on the type of catalytic nanoparticle and etching agent (H_2 gas). Obviously, the appearance of long and straight ZZ and AC nano-trenches indicates that there are two energetically favored directions during the nanoparticle catalytic cutting on *h*-BN. The catalyst-dependent directional cutting behavior (nickel for ZZ trenches and platinum for AC trenches) shown in this experiment indicates that the interaction at the metal-*h*-BN interface is thermodynamically more stable than the H-terminated *h*-BN edge in terms of formation energy.

Due to the binary composition of *h*-BN, the edge configurations of *h*-BN trenches can be either B-rich or N-rich for ZZ edges, or B-N for AC edges, leading to a complicated edge chemistry and metal-BN interfaces. Experimentally, the Ni−ZZ_B interface should have similar thermodynamic stability as the Ni−ZZ_N interface, and both of them are more energetically favorable than the Ni-AC_{BN} interface in optimized experimental conditions. The Pt-AC_{BN} interface is slightly more stable than the Pt−ZZ_B and Pt−ZZ_N interfaces at high temperature and low H_2 gas pressure. In addition, the presence of H_2 gas is essential for catalytic etching of *h*-BN as H_2 can continuously convert the etched B and N atoms from the *h*-BN lattice into BH_x/NH_x/BNH_x.

In these experiments, it is found that the narrower the nano-trench is, the straighter it is. The ultra-narrow trenches are normally created by very small particles produced by extending the annealing duration before the *h*-BN substrates were heated to etching temperature. Recent theoretical investigation [1] reveals that a smaller metal nanoparticle would maximize its contact with either AC or ZZ edges and then move along the more stable metal–AC or metal–ZZ interfaces. This indicates that smaller nanoparticles would be better than larger ones for maintaining a straight cut.

We carried out additional calculations to understand the selective etching of *h*-BN by using Ni and Pt nanoparticles. Previous literature [2] reports that the selective cutting of graphene is along the armchair (AC) or zigzag (ZZ) direction which has strong interactions with the metal nanoparticle. Here, we calculated the interaction strength between *h*-BN edges and the Ni(111) and Pt(111) surfaces by using similar approaches.

To calculate the interfacial formation energy (E_f) between *h*-BN and the catalyst surface, we used *h*-BN nanoribbons with AC and ZZ edges attached to the surface of a three-layer transition metal (111) slab (the (111) surface is the most stable one) to represent the catalyst−BN interface. Another edge of the *h*-BN ribbon (NRs) is terminated by H atoms. The formation energy (E_f) of *h*-BN edge on the transition metal (TM) surface is defined as following:

$$E_f = E(\text{H-BN-TM}) - E(\text{TM}) - E(\text{H-BN}) + E_f(\text{BN-vac}),$$

where E(H‑BN‑TM) and E(TM) are the energies of the whole system and the TM(111) slab, respectively; E(H-BN) is the energy of *h*-BN nanoribbon with one edge saturated by H atoms; L is the length of the TM(111)−BN interface in nanometers; E_f(BN-vac) is the formation energy of

h-BN edge in vacuum and it is calculated by the method used in the reference [1]. Based on the above equation, the E_f of AC and ZZ on Ni(111) and Pt(111) surfaces were calculated, respectively. Considering that the termination atoms on ZZ edge can be B or N atom, the ZZ edge can be further classified as ZZ-B and ZZ-N edges. The formation energy of ZZ-B, ZZ-N and AC edges on Ni(111)/Pt(111) surface are 1.92/-1.07, -2.44/-2.42, -0.23/-1.03 eV/nm, respectively. Considering that the etching of *h*-BN along ZZ direction always results in both ZZ-B and ZZ-N edges simultaneously, we took the average formation energy of ZZ-B and ZZ-N as the formation energy of ZZ edge. Therefore, the formation energies of ZZ and AC on Ni(111)/Pt(111) surface are -0.26/-2.43 and -0.23/-1.03 eV/nm. On both metal surfaces, the formation energy of ZZ are lower than that of AC. The result means both Ni and Pt nanoparticle lead to the etching of ZZ edges.

We also tried the model of edges without any hydrogen atom. Unexpectedly, the formation energy of ZZ is lower than that of AC on both metal surfaces.

We also calculated the interaction strength between *h*-BN edges and the Pt(100) and (110) surfaces by using similar approaches. The large lattice mismatch includes some out-of-plane deformations into the calculation. The results from calculation also show that the formation energy of ZZ is lower than that of AC on Pt surfaces.

It seems that the etching mechanism of Pt nanoparticles in *h*-BN is very complex. Considering that the Ni and Pt nanoparticles have different melting point (Ni:1455°C, Pt:1768°C for bulk), we believe that the different etching behavior of Ni and Pt nanoparticles could be caused by the states of the nanoparticles (e.g. Ni nanoparticles may exist in a liquid phase while Pt nanoparticles could be in a solid state). Besides, the hydrogen pressure plays an important role in the etching. It is found that Ni nanoparticles lead to the etching of some AC oriented trenches in relatively high hydrogen pressure. Extensive investigations along the research direction are still undergoing in our research group. At this moment, we want to leave the question about etching mechanism open to experimental scientists and theorists.

Energy profiles for the growth of GNR at *h*-BN edges

Our experimental results demonstrated that the growth of graphene at the AC edge of *h*-BN is very fast without using any catalyst while the SiH_4 catalyst is required for the fast growth of graphene at the ZZ edges of *h*-BN. To understand the experimental observations, first principles DFT calculations was carried out. The edge configurations of *h*-BN edges can be zigzag boron (ZZB), zigzag nitrogen (ZZN), armchair (AC) edges and the corresponding H-passivated ones, depending on the experimental conditions. **Fig.** S4 shows the calculated phase diagram of ZZB, ZZN, AC and their H-passivated edges. It is clear that ZZB and ZZN can be passivated by H under very low hydrogen pressure, while the AC edge of *h*-BN can be stable even at a very high H pressure. Therefore, the pristine AC edge, H-passivated ZZB and ZZN edges should be the energetically favorable edges at very high temperature in the presence of moderate H_2 pressure. Following calculations about graphene growth will be carried out along these edges.

Based on the configurations of the three edges, we further calculated the energy barriers of graphene growth at the three edges. The activation barrier of graphene growth at the H-passivated ZZB edge is 0.96 eV (**Fig.** S5a), which is much higher than that (0.15 eV) at the AC edge (**Fig.** S7). However, the use of SiH_4 catalyst can reduce the growth barrier to only 0.01 eV (**Fig.** S5b), which greatly promote the growth rate of graphene at the H-passivated ZZB edge. On the other hand, the growth barrier of graphene at the H-passivated ZZN edge is also very high (1.96 eV), as shown in **Fig.** S6a. The use of SiH_4 catalyst can reduce the growth barrier to only 0.37 eV, as shown in **Fig.** S6b. **Fig.** S7 shows the energy profile of graphene growth through the addition of C_2H_2 into the AC edge. It can be seen that the energy barrier for graphene growth at the AC edge is very low (0.15 eV), demonstrating the growth of graphene at the AC edge is very fast even without the SiH_4 catalyst. The use of SiH_4 catalyst can further decrease the growth barrier, making the growth process to be barrierless. Overall, the growth of graphene at the AC edge of *h*-BN is very fast because of the low activation barrier, while graphene growth at the ZZB and ZZN edges are much slower and can be greatly improved by the using of SiH_4 catalyst.

AFM investigation on *h*-BN nano-trenches and GNRs

Extended Data Fig. 2a–d shows examples of ZZ-oriented nano-trenches in *h*-BN substrates. As shown in **Extended Data Fig.** 2a, the nano-trenches mutually exhibit separation angles of 60°, indicating anisotropic etching along a specific crystallographic direction. The inset of **Extended Data Fig.** 2a confirms that the crystallographic orientations of the *h*-BN trenches/edges follow the ZZ pattern. This indicates that the straight nano-trenches along ZZ direction of the *h*-BN sheet are driven by the energetically favored Ni particle-zigzag BN interface. Similar results are shown in **Extended Data Fig.** 1a and 1b. The width distributions of ZZ-oriented trenches in our optimized etching condition are shown in **Fig.** S2a.

Both the width and length of the trenches depend on the process parameters. Nanometre-sized trenches, narrower than 5 nm in width, can be reproduced via optimizing the process (see Supplementary **Table** S1). It might be argued that relatively "blunt" AFM tips would not resolve the exact depth of the narrow trenches and their abrupt height change, but these trenches can be reasonably deduced to be monolayer by measuring wider nano-trenches. Wider nano-trenches (**Extended Data Fig.** 2d) could be obtained by extending the duration of etching or increasing the temperature (Supplementary **Table** S1). The ~78 nm-wide trench in **Extended Data Fig.** 2d had a depth of ~0.340 nm with a bottom roughness comparable to the surface of *h*-BN. The results indicate that the wider trench is mono-layered. The extremely anisotropic two-dimensional (2D) nature of *h*-BN predominantly confined the etching to the top single-atomic layer. Note that the AFM tip size always results in over-estimation of the width of the nano-trenches.

Extended Data Fig. 2e–h presents typical AFM height images of narrow ZGNRs embedded in the nano-trenches of the *h*-BN substrate. Obviously, the GNRs inherit their alignment nature from the templates of the ZZ nano-trenches. For narrow GNRs, out-of-plane height in the range of 20–40 pm can be seen on the surface of the *h*-BN.

Extended Data Fig. 3a–d shows AC-oriented nano-trenches obtained in *h*-BN substrates. As shown in **Extended Data Fig.** 3a, the nano-trenches exhibited mutual separation angles of 60° with no obvious correlation to the direction of the gas flow. Separation angles of odd multiples of 30° were occasionally observed. The white hexagons in the inset of **Extended Data Fig.** 3a help in identifying that the *h*-BN trenches/edges are primarily along AC-direction. This indicates that the crystallographically selective chemical reaction between Pt particles and *h*-BN has a lower activation energy along the AC-direction in *h*-BN. The nano-trenches shown in **Extended Data Fig.** 3a–c are AC-oriented trenches narrower than 5 nm in width. Wider nano-trenches can be obtained by increasing the etching duration (**Table** S2). In **Extended Data Fig.** 3d, it is also found that the ~23 nm-wide trench is mono-layered because it has a depth of ~0.334 nm with a smooth bottom of *h*-BN. Similar to the ZZ trenches, these narrow AC trenches were also reasonably judged to be mono-layered.

Calculation of capacitance and field effect mobility

Field effect transport of transistors made from GNRs grown in *h*-BN was measured. The gate voltage (V_g) dependence of the conductance at different temperatures is plotted in **Fig.** 3 and Supplementary **Fig.** S15-18. The carrier mobility and on-off ratio of each GNR transistor can be extracted from the plots.

According to a classical model, the capacitance is completely determined by the object's geometry and a dielectric constant of the medium. If the object's size shrinks to a nanometer scale, a finite density of state (DOS) which originates from the Pauli exclusion principle should be considered. Low-dimensional systems, having a small DOS, are not able to accumulate enough charge to completely screen the external field. In order to describe the effect of the electric field penetration in a finite DOS system, quantum capacitance should be taken into account. According to theoretical calculations [3], the quantum capacitance can be ignored in devices with a thick dielectric layer. As we are using 300 nm SiO_2 as dielectric layer in these experiments, only classical capacitance is taken into account.

Three-dimensional electrostatic simulation was used to calculate the effective capacitance (C_{gs}) via Fast Field Solvers Software (FFSS), which is available at http://www.fastfieldsolvers.com. The modeled structure includes a large back-gate plane of highly-doped-Si, a dielectric bi-layer with the same lateral dimension as the back-gate (300 nm thickness and dielectric constant ε_0=3.9, for the bottom SiO_2 layer and 10 nm thickness and ε_0 = 4 for the *h*-BN top-layer) and a graphene layer with the experimental dimensions lying ~0.35 nm above the dielectric layer and two metal fingers with the experimental dimensions of the contacts were used to represent them. ~1 nm grids were used for the GNR in a width of *w* (nm) in the simulation. The obtained capacitances are: C_{gs} = 3.71 $pF \cdot m^{-1}$ for a *w* = 5 nm (Supplementary **Fig.** S15 and S18) and C_{gs} = 3.63 $pF \cdot m^{-1}$ for a *w* = 4.8 nm (Supplementary **Fig.** S16). Based on the standard transistor model, the intrinsic carrier mobility is $\mu = \frac{\frac{dG}{dV_{gs}} \cdot L}{C_{gs}}$, where *L* represents the channel length of the GNRs; *G* represents the channel conductance measured. The electrical field mobility can then be derived for the GNR transistors at 300 K (Shown in Supplementary **Fig.** S15-S18).

Simple two band (STB) model

For graphitic materials, a simple two band (STB) model [4-6] is always used to extract the band gap information from the temperature-dependence of the measured resistance. Based on this model, the densities of the electrons (n) and holes (p) are given by $n = C_n k_B T \ln(1+\exp(-\frac{E_C-E_F}{k_B T}))$ and $p = C_p k_B T \ln(1+\exp(-\frac{E_F-E_V}{k_B T}))$, respectively. Here, E_F, E_C, E_V are the energies at the Fermi level, the bottom of the conduction band and the top of valance band, respectively, k_B is the Boltzmann constant and C_n, C_p are constants independent of temperature (T). Ignoring the contribution from static scattering centers, the mobility of the carriers can be expressed as $\mu_e = A_1 T^{-1}$ and $\mu_h = A_2 T^{-1}$, where A_1 and A_2 are constants depending on the strength of the electron and hole-phonon scattering in graphite. Since the resistivity is given by $\rho = (n\mu_e e + p\mu_h e)^{-1}$, the temperature dependence of the resistance can be expressed as:

$$R = \frac{P_1}{\ln(1+\exp(-\frac{E_C-E_F}{k_B T}))+P_2 \ln(1+\exp(-\frac{E_F-E_V}{k_B T}))} + R_{contact}$$

Using E_C-E_F, E_F-E_V, P_1, P_2 and $R_{contact}$ as the fitting parameters, this model fits well with our experimental data for most of the samples at different V_{gate}, as shown in supplementary **Fig.** S15. Based on this model, the energy gap obtained for the ZGNR sample (#Z143) with a width of ~5 nm is 436.2±28.1 meV. And the extracted band gaps are about 183.2±18.7 meV and 530.9±34.7 meV for sample #A39 and #A187, respectively. The model has ruled out a contribution from the contacts.

Discussion on magneto-transport in GNR

The GNRs embedded in *h*-BN provide an ideal experimental subject to investigate the origination of MC behavior in GNR. Imperfect edges are expected to produce significant scattering sources. Sources of disorder such as bulk vacancies, charges in the oxide, or structural deformations are also believed to alter the conductance, although the dominant scattering source remains debated.

In graphene, impurities scatters charge carriers in all possible direction, and then cause a slightly positive MC in a very low magnetic field. The phenomenon is named as weak localization [7,8]. If the spin-orbit interaction is sufficiently large, a quantum interference results in a negative MC behavior in graphene, a phenomenon referred weak anti-localization [9,10].

In GNRs, the positive MC results from a subtle interplay between the specific magnetic band structures and the field-induced reduction in impurity-driven backscattering. In the magnetic field we applied, the size effect of GNRs is dominated as the cyclotron length is greatly larger than the width of GNRs [11]. The charge transport due to the formation of cyclotron orbits originating from Dirac-Landau-level behavior cannot happen in the GNRs.

In narrow ZGNRs, a semiconducting anti-FM spin state theoretically can be excited to the metallic ferromagnetism (FM) state with a high enough magnetic field [12]. However, the semiconducting states in narrow ZGNRs can experimentally survive even at room temperature. Therefore, the magnetic field we applied here is not high enough to break the anti-FM exchange coupling in narrow ZGNR. In addition, the edge states in wide ZGNRs are conductive channels, and cannot be modified in the energy dispersion by external magnetic field. It may be the reason why we found that MC in the ZGNRs (for both Type I and II GNR) is not modified by the perpendicular magnetic field.

In AGNRs, tight-binding calculations have shown that the confinement bandgap of semiconducting AGNRs indeed shrinks continuously with increasing magnetic field [13]. The magnetic field dramatically modifies the energy dispersions and it changes the size of the bandgap, shifts the band-edge states, destroys the degeneracy of the energy bands, induces the semiconductor-metal transition and generates the partial flat bands. This is why the AGNRs exhibits more pronounced MC than ZGNRs does.

In addition, the edge roughness of GNRs and long-range Gaussian potential could cause a positive MC in the magnetic field [14]. The GNRs with more disordered edges or local potential variations have been observed with more pronounced MC [15,16].

It is noted that a relatively large positive MC is observed at low carrier density in AGNRs, and often become saturated at high magnetic field. The reason could be that more channels are available for conduction when higher gate-voltage is applied. The increase in conductance at higher charge density can be attributed to an increase in localization length, due to the increase in the number of occupied transverse channels [17]. In addition, the MC contribution could come from the so-called forward interference between two hopping sites [18]. In this condition, multiple conduction pathways between two points interfere to increase the probability of going from one site to other site, thus generating positive MC, this interference produces a positive MC that saturates at large magnetic field in GNRs.

Although the exact mechanism responsible for the observed difference of GNRs in their MC is not clear at this moment, our experimental findings demonstrate that the ZGNRs exhibit relatively small MC while AGNRs have higher MC. Further experiments well designed and theoretical studies will be carried out to understand the mechanism responsible for the MC behavior in GNRs.

As shown in all atomic resolution STEM images of GNRs, no metal atom is detected in the lattice of GNRs. In addition, all the magneto-transport results are reproducible in all the samples we measured. We believe that there is no influence in MC from the metal residues.

Influence of edge roughness on magneto-transport in edge-specific GNRs

Actually, we can reduce the length of segment with smooth edges in GNRs by modifying the template of *h*-BN nano-trenches. Both ZZ-oriented and AC-oriented GNRs with short smooth segments exhibit similar behavior in their transfer curves and magneto-conductance, which are obviously different from those GNRs with long smooth segments. Based on the results of transport measurement, it is believed that the edge-specific GNRs with long smooth segments embedded in *h*-BN have been successfully fabricated in *h*-BN substrates. The details about the experiments are shown below.

We intentionally changed the partial pressure of hydrogen during etching to obtain *h*-BN nanotrenches with short smooth segments. The flow of H_2 was reduced from 150 to 10 sccm every 3 min for 10 seconds during ZZ-oriented etching, while the flow of H_2 was switched from 10 to 100 sccm every 2 min for 10 seconds during AC-oriented etching, as shown in **Fig.** S28. The unstable etching environment would produce the trenches with short smooth segments. With these templates, GNRs with short smooth segments can be fabricated. The high resolution analysis of the imperfect parts of edge-specific GNRs with short smooth segments are shown in **Fig.** S29.

For sub-5 nm-wide ZZ-oriented GNR samples with short smooth segments, we investigate their electrical properties at different temperatures and magnetic fields. The results are shown in **Fig.** S30. Figure S30a shows conductance (G) as a function of V_{gate} at room temperature and 2 K of the typical ZZ-oriented GNR FET with short smooth segments. Its channel length l is ~240 nm and the width w is ~5 nm. The ZZ-oriented GNR device shows about 3 orders lower conductivity of on-state and much lower mobility than those ZGNRs with long smooth segments. The on-state conductance is $\sim 5\times10^{-3}$ e^2/h at 300 K. And the GNR shows suppressed conductance over a wide range (from -65 to 50 V) in the G-V_{gate} characteristics at 2 K, with some fluctuations observed inside. Such effects are always attributed to transport gap resulting from edge roughness, similar behavior has been observed in lithographic GNRs [19] and graphene nano-constrictions [20]. Theoretical calculations [21] have shown that the density of states of GNRs with rough edge are dominated by localized states, and the charge transport could be through hopping between these localized states at low temperature.

Figure S30b shows G as a function of V_{gate} under different magnetic fields perpendicular to the substrate at 2 K. Although the conductance still shows fluctuations in the whole gate range, the GNR shows a very large positive MC near the minimum conductance. Upon applying a magnetic field, the overall conductance increases dramatically, with a reduced transport gap (from -30 to 35 V). These results suggest that the transport scattering decreases with increasing magnetic field.

Figure S30c shows the magneto-transport properties of the ZZ-oriented GNR device, a huge positive MC (more than a factor of 10,000) is found at 2 K. It is clear that the conductance is essentially switched on from an off-state. And it is also found that all the MCs are positive at all V_{gate} and there is no trend for saturation of the MCs. The large MC normally appears near the suppressed transport gap regime.

Similarly, we also investigated the electrical transport of AC-oriented GNRs with short smooth segments. The results are shown in **Fig.** S31. Figure S31 shows the electrical transport properties of an AGNR with short smooth segments. Its channel length l is ~220 nm and a width w of ~5 nm.

As **Fig.** S31a shows, the on-state conductance is ~0.005 e^2/h and the transport gap is more than 60 V even at 300 K. Figure S31b shows that the conductance of the AGNR can also be tuned by the magnetic field. And the value of MC is also very large at the suppressed transport gap regime. As **Fig.** S31c shows, the MCs are also positive and large at all the gate biases. And a huge positive MC of ~10,000 is occurred at V_{gate} = -30 V at 9 T. All the transport behavior is quite similar to the ZZ-oriented GNR with short smooth segments.

Both ZGNRs and AGNRs with short smooth segments include much more mixed edges and then have higher edge roughness, the GNR would like to behave as a series number of quantum dots with large numbers of localized sites, which may cause a low conductivity. The edge roughness induced back-scattering, in terms of strong localization, may contribute to the observed conductance suppression and which is more sensitive to the magnetic field. And this is the reason why the sub-5 nm-wide ZGNRs and AGNRs with short smooth segments show similar transport behavior.

In addition, we also studied the electronic properties for wider GNRs w ~ 10 nm. The results are shown in **Fig.** S32 and S33.

As shown in **Fig.** S32a, the on-state conductance of the ZGNR device (channel length l of ~245 nm) is ~ 0.09 e^2/h, which is higher than the sub-5 nm-wide ZGNR device. The transport gap is about 40 V at 4 K. Figure S32b shows the transfer curves for the device subjected to different B at 4 K. It also can be found that the B can tune the conductance and the factor is much smaller when the device is gated far away from the transport gap. Figure S32c shows the MCs at different V_{gate} at 4 K. The relatively large positive MC ~2,000 is observed when the B is at 9 T and the gate voltage is set to 0 V.

Comparison to the ~10 nm-wide ZGNR with short smooth segments, the 10 nm-wide ZGNR with long smooth segments show a much higher on state conductance. Significantly, the weak metallic conductance peak which is related to the zigzag edge is not detected which means the roughness of ZGNR edge increases. Besides, the MCs in ZGNRs are 2-3 orders higher than those in ZGNRs with long smooth segments. Apparently, in this case, the huge MC behavior attributes to increase of edge roughness.

Similarly, we also carried out the transport measurement of low quality AGNR FET with w ~ 10 nm. The results are shown in **Fig.** S33. The channel length l of ~228 nm. As shown in **Fig.** S33a, the on-state conductance is a ~0.2 e^2/h at 300 K and ~0.015 e^2/h at 4 K. And the transport gap at 4 K is about 30 V. The magnet filed can also tuned the conductance at 4 K (**Fig.** S33b). Figure S33c shows that a relatively large positive MCs is obtained at all V_{gate}.

We plot all values of MC obtained under $B_{//z}$ = 9 T at different V_{gate} for all GNR samples in **Fig.** S34. As shown in **Fig.** S34, MCs in ZGNRs with short smooth segments become very large, and the values are quite similar to those in AGNRs with short smooth segments. Some of them are higher than 10E5, as shown in **Fig.** S34a. The large MC mainly comes from scattering of rough edges to charge carriers in both ZGNRs and AGNRs with short smooth segments. Both the ZGNRs and AGNRs with short smooth segments show much larger positive MCs than GNRs with longer smooth edges, the results are believed to be related to edge roughness.

In summary, both ZGNR and AGNR with short smooth segments show much lower on state conductance and wider transport gap than those with long smooth segments. For ZGNR with short smooth segments, both the sub-5 nm-wide and 10 nm-wide ZGNRs show 2-3 orders lower on-state conductance and 2 orders higher MC than those with long smooth segments when the magnetic field is applied to 9 T. Besides, a pronounced conductance peak is absent in 10 nm-wide ZGNRs with short smooth segments while that is always observed in those ZGNRs with long smooth segments. For AGNR, on-state conductance in AGNRs with short smooth segments becomes 2-3 orders lower than those with long smooth segments, and their MCs increase 2-3 orders higher than those with long smooth segments. It is also found that the MCs of ~10 nm-wide AGNR don't show any trend of saturation which happens in AGNRs with long smooth segments.

Raman Spectra of GNRs

Raman measurements were carried out to investigate the structural and electronic properties of the ultra-narrow AGNR and ZGNR on *h*-BN. All the data were collected using an exciting laser of 532 nm. **Fig.** S39 shows the Raman spectra. In all spectra shown in **Fig.** S39, a prominent sharp peak appeared at ~1,366 cm^{-1}, which was attributed to the Raman-active LO phonon of *h*-BN [22]. For the spectra of the GNRs, the G-, D- and 2D-bands were fitted with a single-Lorentzian line shape. In the spectrum of the AGNR (azure line), the D-band appeared at 1336.0 cm^{-1}, and G-band at 1594.3 cm^{-1}, and the inset shows an enlarged 2D-band of the AGNR(~2,654.7 cm^{-1}). In the spectrum of ZGNR (red line), the D band appears at 1,344.2 cm^{-1}, the G-peak at 1,594.8 cm^{-1} and the 2D-peak at ~2,671.3 cm^{-1}. Raman spectra confirm that the narrow GNRs consist of sp^2 carbon. In addition, the observed broadening of the full width at half-maximum for the Raman G- and 2D-bands in both AGNR and ZGNR may be due to strain variations at the nanometre-scale [23]. It is obvious that the D peak in AGNR exhibits much stronger intensity than that of ZGNR because the defect-assisted double resonant inter-valley scattering process only occurs at armchair edges and is forbidden at the zigzag edge [24]. The tiny D band in ZGNR may come from imperfections in the zigzag edges. In most cases, a ZGNR is comprised of series of perfect zigzag segments. The average length of the straight segments can be estimated by measuring the mean free path of charge carriers from transport measurement.

References

1 Ma, L. & Zeng, X. C. Catalytic directional cutting of hexagonal boron nitride: The roles of interface and etching agents. *Nano Lett.* **17,** 3208–3214 (2017).

2 Ma, L., Wang, J. L., Yip, J. & Ding, F. Mechanism of transition-metal nanoparticle catalytic graphene cutting *J. Phys. Chem. Lett.* **5,** 1192−1197 (2014).

3 Shylau, A. A., Kłos, J. W. & Zozoulenko, I. V. Capacitance of graphene nanoribbons. *Phys. Rev. B* **80,** 205402 (2009).

4 Kelly, B. T. *Physics of Graphite* (Applied Science, London, 1981).

5 Ebbesen, T. W. *Carbon Nanotubes: Preparation and Properties* (CRC Press, Boca Raton, FL, 1997).

6 Wang, H., Choong, C., Zhang, J., Teo, K. L. & Wu, Y. Differential conductance fluctuation of curved nanographite sheets in the mesoscopic regime. *Solid State Commun.* **145,** 341 (2008).

7 Tikhonenko, F. V., Horsell, D. W., Gorbachev, R. V. & Savchenko, A. K. Weak localization in graphene flakes. *Phys. Rev. Lett.* **100,** 056802 (2008).

8 Licini, J. C., Dolan, G. J. & Bishop, D. J. Weakly localized behavior in quasi-one-dimensional Li films. *Phy. Rev. Lett.* **54,** 1585 (1985).

9 Kumar, C. et al. Localization physics in graphene Moire superlattices. *Phys. Rev. B* **98,** 155408 (2018).

10 Wu, X., Li, X., Song, Z., Berger, C. & de Heer, W. A. Evidence for weak antilocalization in epitaxial graphene. *Phys. Rev. Lett.* **98,** 136801 (2007).

11 Peres, N. M. R., Castro Neto, A. H. & Guinea, F. Dirac fermion confinement in graphene. *Phys. Rev. B* **73,** 241403 (2006).

12 Son, Y.-W., Cohen, M. L. & Louie, S. G. Half-metallic graphene nanoribbons. *Nature* **444,** 347 (2006).

13 Huang, Y. C., Chang, C. P. & Lin, M. F. Magnetic and quantum confinement effects on electronic and optical properties of graphene ribbons. *Nanotechnology* **18,** 495401 (2007).

14 Han, M. Y., Brant, J. C. & Kim, P. Electron transport in disordered graphene nanoribbons. *Phys. Rev. Lett.* **104,** 056801 (2010).

15 Evaldsson, M., Zozoulenko, I. V., Xu, H. & Heinzel, T. Edge disorder induced Anderson localization and conduction gap in graphene nanoribbons. *Phys. Rev. B* **78,** 161407R (2008).

16 Li, T. C. & Lu, S.-P. Quantum conductance of graphene nanoribbons with edge defects. *Phys. Rev. B* **77,** 085408 (2008).

17 Javey, A., Guo, J., Wang, Q., Lundstrom, M. & Dai, H. Ballistic carbon nanotube field-effect transistors. *Nature* **424,** 654-657 (2003).

18 Mucciolo, E. R., Castro Neto, A. H. & Lewenkopf, C. H. Conductance quantization and transport gaps in disordered graphene nanoribbons. *Phys. Rev. B* **79,** 075407 (2009).

19 Stampfer, C. et al. Energy gaps in etched graphene nanoribbons. *Phys. Rev. Lett.* **102,** 056403 (2009).

20 Todd, K., Chou, H.-T., Amasha, S. & Goldhaber-Gordon, D. Quantum dot behavior in graphene nanoconstrictions. *Nano Lett.* **9**, 416 (2009).

21 Querlioz, D. et al. Suppression of the orientation effects on bandgap in graphene nanoribbons in the presence of edge disorder. *Appl. Phys. Lett.* **92,** 042108 (2008).

22 Geick, R., Perry, C. H. & Rupprech, G. Normal modes in hexagonal boron nitride. *Phys. Rev.* **146,** 543 (1966).

23 Neumann, C. et al. Raman spectroscopy as probe of nanometre-scale strain variations in graphene. *Nat. Commun.* **6,** 8429 (2015).

24 You, Y., Ni, Z., Yu, T. & Shen, Z. Edge chirality determination of graphene by Raman spectroscopy. *Appl. Phys. Lett.* **93,** 163112 (2008).